Performance and error budget of a GLAO system

Andrei Tokovinin

Cerro Tololo Inter-American Observatory, Casilla 603, La Serena, Chile

ABSTRACT

Reliable prediction of the image quality delivered by a ground-layer AO (GLAO) system can be made using several methods, given the parameters of the instrument and the statistics of the turbulence profile above the observatory. Extensive data accumulated over several years at different sites indicate that GLAO can bring a significant gain in performance for classical astronomical observations, and at visible wavelengths. This gain can become spectacular on nights with calm upper atmosphere that happen infrequently but regularly at all sites studied so far. Starting from an ideal GLAO system, the influence of various instrumental errors (wave-front sensing, time delay, tilt, optics ripple, etc.) is studied, leading to the formulation of an error budget for GLAO. As the performance metrics of GLAO and classical AO are very different, we propose a new criterion for balancing error contributions.

Keywords: Adaptive Optics

1. INTRODUCTION

Adaptive optics is revolutionizing ground-based astronomy at near-IR wavelengths.[1] In the visible, most observations are still seeing-limited. The diffraction limit can be achieved on bright stars with specialized (ExAO) instruments. Meanwhile, even partial compensation of turbulence can offer a substantial gain over seeing. Ground-Layer Adaptive Optics (GLAO) is especially attractive. By compensating selectively only low-altitude turbulence, GLAO achieves correction over a field of several arc-minutes, enhancing the capabilities of ground-based telescopes doing classical astronomy (imaging, spectroscopy). The ground-layer (GL) turbulence is, typically, slower than high-altitude turbulence, and it is easier to sense and to compensate. A ring of laser guide stars (LGSs) surrounding the science field appears to be the optimal sensing configuration. A single low-altitude Rayleigh LGS is also suitable for selective GL sensing and is a simpler alternative to more ambitious geometries. This approach is adopted for the SOAR Adaptive Module (SAM) instrument[2] and for the GLAS system.[3]

If the optical turbulence profile (OTP) $C_n^2(h)$ is known, we can calculate the gain in resolution which would result from compensating all turbulence below a chosen altitude H_0. This naive estimate does not take into account many factors. Turbulence below H_0 will be corrected only partially, while some correction above H_0 will be done, too. The Point Spread Function (PSF) of the GLAO system depends on the choice of H_0 and on the OTP, and it varies across the field. By decreasing H_0, we achieve compensation in a wider field, but obtain less gain in resolution. The shape of the GLAO-corrected PSF is different from the seeing-limited PSF, with a more prominent core and substantial halo. Therefore, adequate tools for predicting reliably the GLAO PSF and its potential gain over seeing are needed. In this paper, I review the tools for PSF calculation in GLAO and its predicted performance, drawing examples from the SAM instrument.

The suite of tools for GLAO analysis must be complemented with an evaluation of the instrumental errors which diminish the gain. System engineering and trade studies of GLAO require an error budget. The standard AO approach of quantifying residual errors in terms of Strehl ratio does not work for GLAO, we need alternative ways to evaluate the impact of instrument imperfections on the compensated PSF. I propose here to constrain the errors by the values of the associated wave-front structure function at some relevant baseline, say 0.5 m.

E-mail: atokovinin@ctio.noao.edu

2. GLAO PERFORMANCE

2.1 Methods

The ultimate aim of a classical AO system is to obtain a perfect wave-front. So, any residual wave-front deviations ϵ are considered as errors. The AO error budget is usually formulated in terms of the residual rms error σ_ϵ, which is directly related to the Strehl ratio $S = \exp[-(2\pi/\lambda)^2 \sigma_\epsilon^2]$, where σ_ϵ is measured in units of length and $(2\pi/\lambda)$ converts it to radians for the imaging wavelength λ.

In GLAO, the diffraction limit is never reached, $\sigma_\epsilon > \lambda$, so this quantity does not characterize the performance. Instead, we are interested in the corrected PSF and its parameters, such as Full Width at Half Maximum (FWHM), ellipticity, energy concentration, peak intensity, etc. One obvious method to evaluate the PSF is by Monte-Carlo simulation. However, this approach is computationally intensive and lacks the flexibility needed to explore the trade space of multiple instrumental parameters and varying atmospheric conditions.

A better approach is to derive the long-exposure PSF from the *second-order statistics* of the wave-front residuals. The basic relation between the Optical Transfer Function $T(\mathbf{f})$ (OTF, a Fourier transform of the PSF) and the structure function (SF) of the residuals $D_\epsilon(\mathbf{r}) = \langle [\epsilon(\mathbf{r}_1 + \mathbf{r}) - \epsilon(\mathbf{r}_1)]^2 \rangle$ is well known,[4]

$$T(\mathbf{f}) = T_0(\mathbf{f}) \exp[-0.5(2\pi/\lambda)^2 \bar{D}_\epsilon(\lambda \mathbf{f})]. \tag{1}$$

Here $T_0(\mathbf{f})$ is the OTF of the telescope, possibly including non-common-path aberrations, $\mathbf{f}$ is the spatial frequency vector, $\mathbf{r} = \lambda \mathbf{f}$ is the coordinate on the pupil. The statistics of phase residuals changes across telescope aperture, but the aperture-averaged SF $\bar{D}_\epsilon(\mathbf{r})$ takes this into account and depends only on one spatial coordinate $\mathbf{r}$. The Eq. 1 is an approximation which was shown[4] to be acceptably good for low-order AO systems and is even better at high orders.

The residual SF is a key element in estimating GLAO performance. It enters in the computation of the PSF through the exponent in Eq. 1. At small baselines $\mathbf{r}$ the SF is close to zero, the exponent is close to one. On the other hand, at large $\mathbf{r}$ the OTF is nearly zero because $(2\pi/\lambda)^2 D_\epsilon(\mathbf{r}) \gg 1$. Only the range of baselines where $D_\epsilon(\mathbf{r}) \sim (\lambda/2\pi)^2$ really matters for the calculation of the OTF and PSF. It is shown in Ref. 6 that this critical baseline is of the order of $\lambda/2\beta$ for an imaging wavelength λ and final image FWHM β. Assuming $\lambda = 0.7\mu m$ and $\beta = 0.2''$, this baseline is 0.36 m. Thus, we need good estimates of the residual SF only at baselines $\sim$0.5 m and shorter.

The fraction of energy $E(\beta)$ concentrated in a circle of some angular diameter β can be calculated directly from the PSF. However, an alternative and more accurate method uses the OTF by noting that the Fourier transform (FT) of the circle is an Airy function $A(x)$. The integral of the PSF over circle is expressed in the Fourier domain as a convolution product, therefore the encircled energy $E(\beta)$ equals

$$E(\beta) = \left[\int A(\beta|\mathbf{f}|) \mathrm{d}\mathbf{f} \right]^{-1} \int A(\beta|\mathbf{f}|) T(\mathbf{f}) \mathrm{d}\mathbf{f}, \quad \text{where} \quad A(x) = \frac{2J_1(\pi x)}{\pi x}. \tag{2}$$

We checked this method against direct PSF integration. The OTF method is to be preferred because it is less affected by the pixel sampling. The Airy function crosses zero at a baseline $r = 1.22\lambda/\beta$ or 0.59 m for $\lambda = 0.7$ μm and $\beta = 0.3''$. This confirms the above estimate of relevant baselines for evaluating GLAO performance.

2.2 PSF estimation by modal covariance

This method follows the original development by Véran el al.[4] coupled with the modal covariance analysis of MCAO systems.[5] The residual phase on the telescope pupil of radius R can be represented by a sum of Zernike polynomials $Z_j(\mathbf{r}/R)$ with coefficients c_j,

$$\epsilon(\mathbf{r}) = \sum_{j=2}^{\infty} c_j Z_j(\mathbf{r}/R). \tag{3}$$

The $j = 1$ mode (piston) is explicitly excluded. The coefficients c_n of the residual error are random variables with a second-order statistics depending on the atmospheric turbulence and on the AO system characteristics. We denote the corresponding covariance matrix by $C_{ij} = \langle c_i e_j \rangle$. The residual SF can then be expressed as

$$\bar{D}_\epsilon(\mathbf{r}) = \sum_{i=2}^{\infty} \sum_{j=2}^{\infty} C_{ij} U_{ij}(\mathbf{r}), \tag{4}$$

where $U_{ij}(\mathbf{r})$ are called "mode shape functions". They equal suitably normalized integrals of Zernike polynomial's products over the aperture.[4] These functions need be pre-computed only once. Their number is large: by limiting the Zernike expansion to J terms, we still need $(J-1)(J-2)/2$ functions, or 946 for $J = 45$. The task is simplified by computing U_{ij} only within ± 1m from the coordinate origin because their values at larger distances have no influence on the PSF in the case of GLAO, and by using a coarse sampling with subsequent interpolation. The recipe for calculating residual covariances C_{ij} is given in Ref. 5. It needs only a minor modification in the case when tilts of several natural guide stars (NGSs) are averaged.

2.3 PSF estimation by analytic method

A different approach to calculating the PSF in GLAO is developed in Ref. 6. It is based on FT and is very fast. Good agreement with Monte-Carlo simulations has been demonstrated.[7] The analytic method uses the actuator pitch d instead of the radial compensation order n. By setting $d = 1.1D/n$ (D – telescope diameter), we can compare analytic and modal methods.

The development of the analytic GLAO code led to splitting the task of PSF computation into several stages.[6] At first, a "library" of the normalized residual SFs is calculated for a given system geometry and for the selected test points in the field. This stage is most intensive computationally (but still much faster than the modal code). Then the SFs are combined with different OTPs, scaled to a given imaging wavelength, and converted to PSFs. This last stage is so fast that thousands of profiles can be processed in a matter of minutes. The same approach works with the modal code, of course.
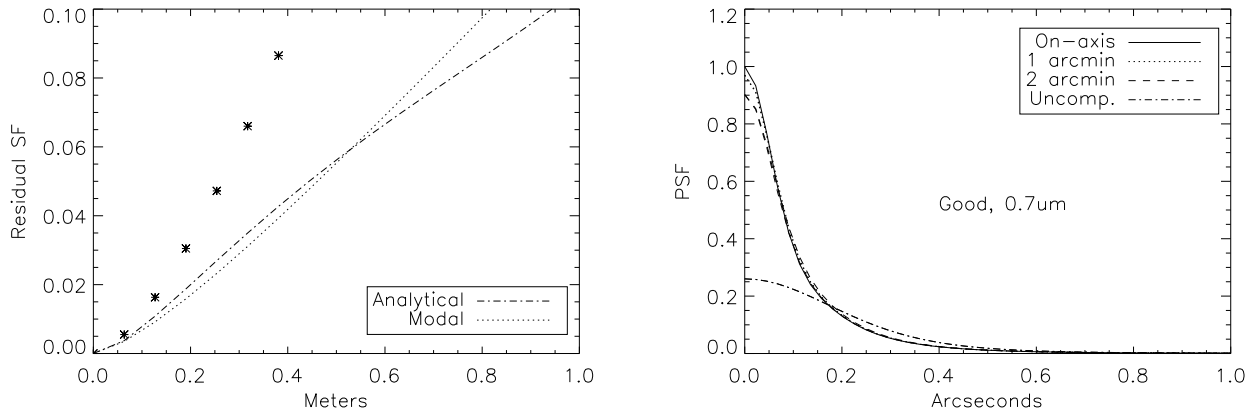
Figure 1. **Left:** Comparison of the residual SFs (normalized, as a function of the baseline) computed by the modal code (dotted) and by the analytic code (dash-dot) for the compensation up to radial order 8 (45 Zernike modes) and a single turbulent layer at 2 km, with LGS at 10 km and two tip-tilt stars at $\pm 2.5'$ from the center. **Right:** Cuts of the PSFs in two directions, x and y, in the field center and at 1 and 2 arcmin. radii. Wavelength 0.7 μm, good conditions (see below), observations at zenith. The un-compensated PSF is plotted for comparison.

Figure 1 (left) shows a comparison between modal and analytic methods of SF calculation for the case of a single Rayleigh LGS and a single turbulent layer at 2 km from the telescope. The asterisks denote the un-compensated atmospheric SF. Although in this case the effective actuator size is only $d = 0.6$ m, the residual SFs are lower than the un-compensated SF at baselines much smaller than d. Consequently, the OTF and PSF are improved even in the visible ($r \sim 0.2$ m). This beneficial effect of low-order compensation is well known,

it explains why even a relatively low-order GLAO system improves the PSF at visible wavelengths. Figure 1 (right) gives an example of the compensated PSFs for the SAM instrument under good atmospheric conditions (see below), at three positions in the field, to illustrate the resolution gain provided by GLAO.

3. TURBULENCE PROFILES AND CALM NIGHTS
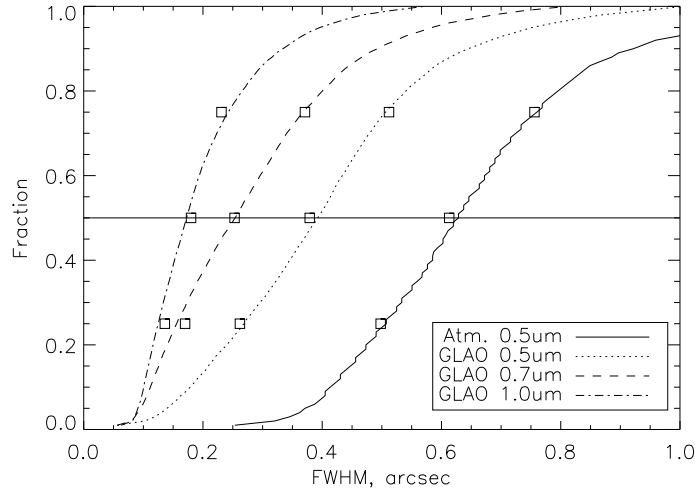
Figure 2. Cumulative distributions of the FWHM of seeing-limited PSF at 0.5 μm and SAM-compensated FWHM at three wavelengths (on-axis). The values derived from the OTP models are plotted as squares.

The performance of any AO system critically depends on the atmospheric parameters, mostly on the *optical turbulence profile* (OTP) $C_n^2(h)$ and on the wind speed $V(h)$ (the AO time constant τ_0 combines OTP with wind). The performance is usually estimated for some representative (e.g. median) OTP. However, when an astronomer actually uses the AO, the conditions will be variable and, generally, different from the typical ones. How relevant are the estimates calculated for typical OTP models?

The rapidity of the analytical PSF estimation and the large number of low-resolution OTPs measured with the MASS-DIMM monitors[8] enable detailed predictions of the GLAO (and AO) PSFs as a function of time, wavelength, zenith distance, and source position in the field. The large number of input and output parameters make such predictions difficult to digest, however. They can be treated statistically. Figure 2 shows the histogram of on-axis FWHM in the SAM instrument at three wavelengths for the period of 4 months, based on 6531 individual measured OTPs. Statistically, the resolution is improved by GLAO not only under median or good conditions, but almost always.

Figure 3 plots the variation of SAM-corrected PSF during two nights. The first one, with calm upper atmosphere, shows the most spectacular gain at all wavelength, while on the second night, only 10 days later, the expected gain would be much more modest, although still non-negligible. As the conditions degrade, the GLAO gain decreases stronger at shorter wavelengths, where the PSF variability is also more pronounced. This difference is mostly caused by the limited compensation order of SAM. With a high-order GLAO system, the performance at short wavelengths would improve, and there will be less PSF variability. The difference between the 0.5 μm and 1 μm histograms in Fig. 2 would be much smaller, too.

Histograms like those in Fig. 2 can be constructed for other relevant performance metrics, but they would still not show the correlations between those metrics. Moreover, it is difficult to optimize the GLAO system parameters in this way, so we still need OTP *models*! Three models representative of the best 25%, median, and 75% conditions at Cerro Pachón were proposed in Ref. 9 to approximate the performance of a specific GLAO system, SAM (squares in Fig. 2). This is a step forward compared to the single typical OTP used previously. For some other AO systems, these models may prove inadequate and will need adjustment.
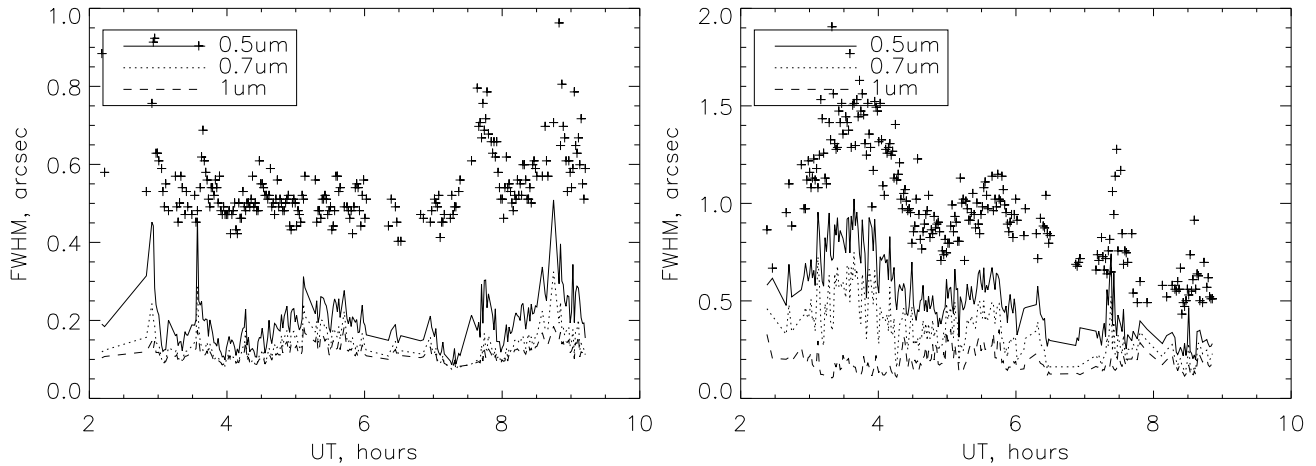
Figure 3. Variation of the PSF FWHM in SAM at three wavelengths (0.5, 0.7, and $1\,\mu$m) as a function of time for two nights. The atmospheric seeing is plotted as crosses.
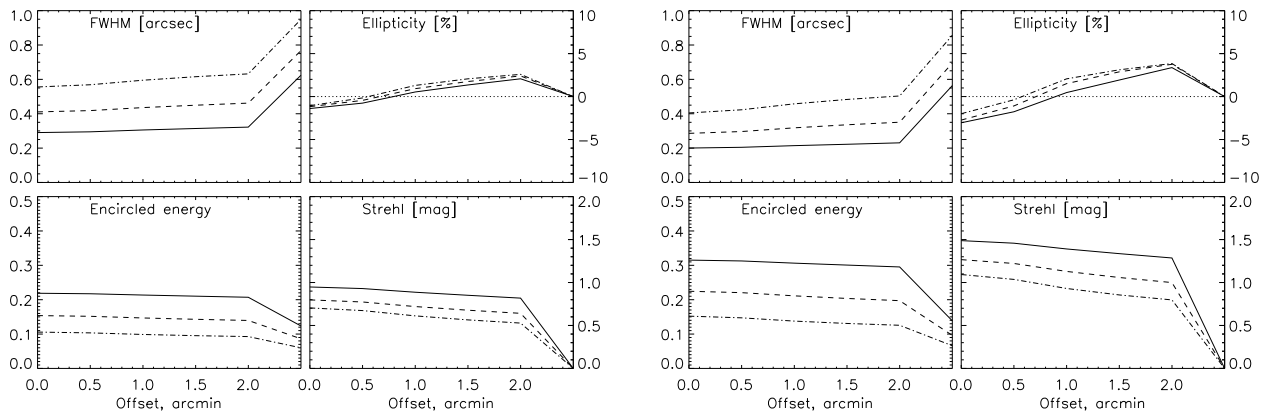
Figure 4. Parameters of the SAM PSF at $500\,$nm (left) and $700\,$nm (right) wavelengths across the field. The solid, dashed and dash-dotted lines correspond to the good, typical and bad conditions, respectively. Zenith distance $45°$. The un-corrected seeing-limited performance metrics are plotted at $2.5'$ offset.

Armed with the OTP models. we can present the expected GLAO performance in a more concise way. For example, Fig. 4 gives the variation of different PSF metrics over the field, with the last point representing the un-corrected PSF. Such plots inform a potential user on the range of performance variations caused by changing conditions.

Nights with calm upper atmosphere deserve particular attention. According to the OTP statistics at Cerro Pachón,[9] the free-atmosphere seeing is better than $0.29''$ for 25% of the time, reaching values as small as $0.15''$. On all sites surveyed so far with MASS such calm nights happen regularly. The gain of using GLAO on such nights will be spectacular (cf. Fig. 3, left), no less than at the Antarctic sites. There is no need to wait for telescope construction in Antarctica to access the unique science potential offered by the existing large telescopes. It is only a matter of planning. Flexible scheduling based on the total seeing is a reality at some observatories, but AO (and, especially, GLAO) needs such scheduling on the basis of the free-atmosphere seeing.

4. GLAO ERROR BUDGET

4.1 Definition of errors

Even a perfectly working GLAO system does not compensate all turbulence, so $\epsilon \neq 0$. It does not make sense then to consider σ_ϵ as a metric of instrumental performance, as in the classical AO. Instead, we split the residual
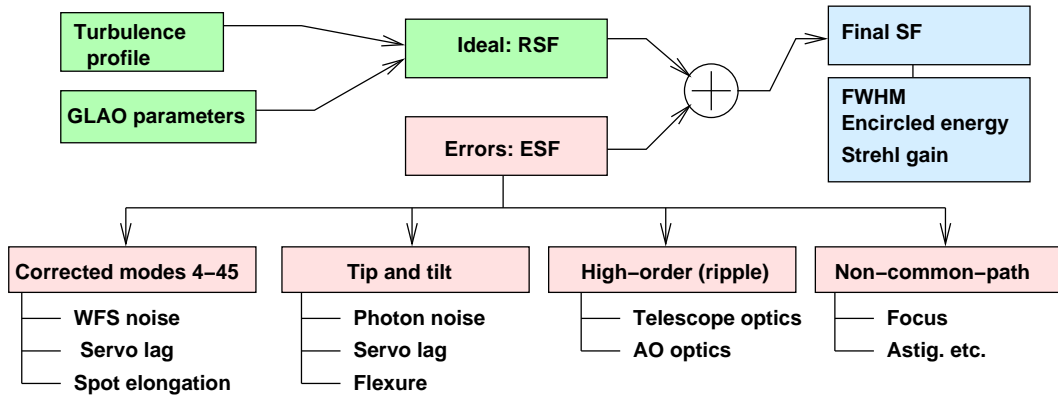
Figure 5. Top-level diagram of GLAO error budget.

wave-front errors in two parts: those arising from the uncompensated turbulence and those caused by the GLAO instrument imperfections such as noise, servo lag, etc.

Each error component is independent of the atmospheric residuals and of other errors and can be described statistically by its *error structure function* (ESF) $D_{\epsilon,err}(\mathbf{r})$. We have to add these terms to the atmospheric *residual structure function* (RSF) $D_{\epsilon,atm}(\mathbf{r})$ of an ideal instrument and use the sum in Eq. 1 to calculate the OTF and PSF. In other words, instrumental errors reduce the OTF by an additional multiplicative factor and broaden the PSF accordingly. For example, tilt errors in the x-direction with dispersion σ_{tilt}^2 add a quadratic term $D_{\epsilon,tilt}(x,y) = \sigma_{tilt}^2 x^2$ to the ESF and broaden the PSF in x-direction by convolution with a Gaussian of rms width σ_{tilt} radian.
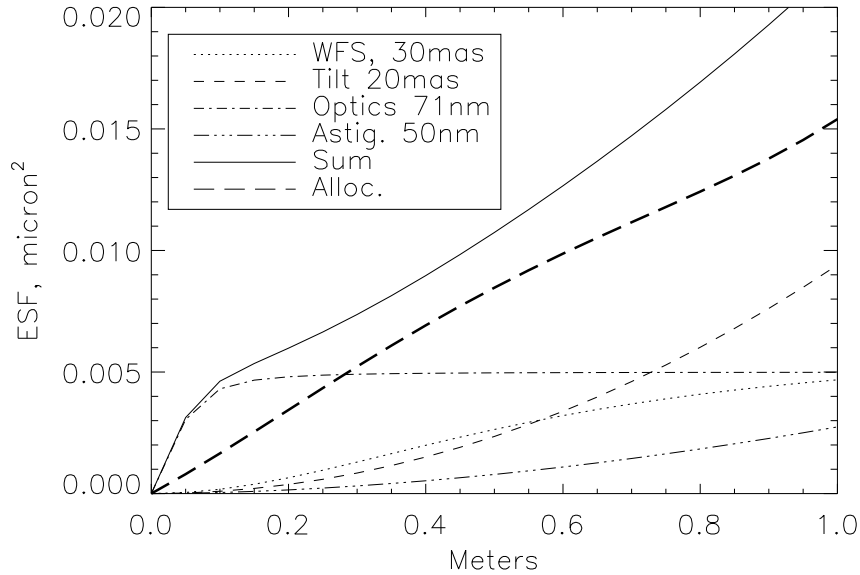
Figure 6. Different components of the ESF and their sum. The thick long-dash line marks the allocation (10% of $D_{\epsilon,atm}$ for typical conditions). The numbers show the parameters assumed in the calculation: WFS centroid rms noise 30 mas, tilt noise 20 mas, small-scale optical errors 71 nm rms, non-common-path aberration (astigmatism) of 50 nm rms.

Figure 5 shows schematically our approach to the error budget of GLAO. The errors of the corrected modes (with tilt considered separately) are the usual worry of an AO system designer who tries to balance various conflicting requirements. In addition to this, the effects of small-scale errors of the optical surfaces (ripple) and

non-common-path errors turn out to be non-negligible and should be included in the overall budget.

The acceptable level of instrumental errors is determined by their influence on the compensated PSF. We do not want to sacrifice the gain of an ideal GLAO system and therefore allocate only a certain small fraction F of the atmospheric residuals to the instrumental errors,

$$\sum_k D_{\epsilon,err\ k}(\mathbf{r}) < F\ D_{\epsilon,atm}(\mathbf{r}). \tag{5}$$

This condition needs not to hold at all baselines $\mathbf{r}$ because the PSF is influenced only by the ESF at $|\mathbf{r}| \leq 0.5\,\mathrm{m}$ (see above). If we want to describe the contributions of each error source in GLAO by one number, $D_{\epsilon,err}(0.5\mathrm{m})$ will be a good choice. The allocation depends on the observing conditions. In the case of SAM, $D_{\epsilon,atm}$ is almost a linear function of $|\mathbf{r}|$, and it roughly increases by 1.5 times when going from typical to bad conditions, and diminishes by the same factor under good conditions. So, by allocating a factor F to instrumental errors, we increase the FWHM approximately by $1 + F$ times.

Figure 6 shows the preliminary error budget for SAM, assuming typical conditions and $F = 0.1$. In fact, the sum of all error terms slightly exceeds the allocation. At baselines shorter than $0.2\,\mathrm{m}$, the optics ripple strongly dominates over all other sources. Although the optics of the SOAR telescope has a very high, state-of-the art quality, it was fabricated with a small polishing tool, so the residual small-scale errors cannot be removed either by the active optics of the telescope or by the SAM instrument. The contribution of the ripple in the SAM instrument has been included, but it is probably over-estimated at this stage. At large baselines, on the other hand, the quadratic ESF caused by tilt errors dominates over other errors.

4.2 Errors of corrected modes

If the modal coefficients in a *real* GLAO instrument contain some additional errors and these errors are uncorrelated with atmospheric residuals in a perfect instrument, their contribution to the ESF can be calculated by Eq. 4 using the covariance matrix of modal errors C. We consider three mutually independent sources of modal errors: the reconstructor errors, WFS measurement noise, and servo lag.

Reconstructor errors exist in any AO system. Spot centroids in the WFS (vector $\mathbf{X}$ expressed as linear wave-front differences across sub-apertures) are related to the vector of modal coefficients $\mathbf{Z}$ by the gradient matrix G, $\mathbf{X} = G\mathbf{Z}$. The modal coefficients are obtained from $\mathbf{X}$ by applying an inverse *reconstructor matrix G^**, $\mathbf{Z} \approx G^*\mathbf{X}$. The reconstructor is never perfect. It can be intentionally made "softer" to reduce noise propagation at the expense of accuracy (cf. Ref. 1, Ch. 5 and Ref. 10). Knowing the reconstructor and the statistics of atmospheric Zernike coefficients, it is trivial to evaluate the covariance matrix of associated errors:

$$C_{rec} = (\lambda/2\pi)^2\ (D/r_0)^{5/3}\ EC_\phi E^T, \quad \text{with} \quad E = I - G^*G. \tag{6}$$

Here D is the telescope diameter, r_0 is the effective Fried parameter, C_ϕ is the Noll's covariance matrix of Zernike coefficients for $D/r_0 = 1$, I is the identity matrix. Estimates show that the reconstructor errors are much smaller than other errors such as higher-order modes, so the optimization of the reconstructor is not critical.

WFS noise in one loop cycle depends on the detected LGS flux, detector noise, and spot elongation. The flux is proportional to the loop time and elongation and also depends on the LGS power, range, and zenith distance. The WFS noise propagates into the modal coefficients and is filtered by the servo loop temporal response. So, C_{noise} depends on many parameters in a complex way.

We begin the analysis by determining the centroid errors of LGS spots in a S-H WFS. Assuming a weighted centroid algorithm, the formulas given in Ref. 11 are generalized to radially-elongated spots. In this case the centroid errors in x and y are correlated. The elongation is quantified by the relative elongation parameter $l = 0.48\Delta/\beta$, where $\Delta = LD/(2H)^2$ is the angular extent of the LGS plume as seen from the edge of telescope aperture (diameter D) for the range gate L and LGS distance H, and β is the FWHM size of (Gaussian) spots determined by turbulence on up-link and down-link paths and diffraction. The centroid errors are propagated

to the modal coefficient errors by means of the reconstructor matrix, as usual: $C_{noise} = G^* C_X (G^*)^T$, and the ESF is calculated with Eq. 4. It turns out that the result can be well approximated with only two parameters:

$$D_{\epsilon,noise}(r) \approx 2.7\sigma^2 \frac{(r/r_1)^2}{1 + (r/r_1)^2}, \tag{7}$$

where σ^2 is the total variance of all corrected modes and r_1 is the characteristic scale, of the order of the actuator size.

It is convenient to describe the WFS noise by a single parameter σ_0 (centroid error for round spots or in tangential direction, in μm or other linear units) and to include the effects caused by the elongation as part of the noise propagation matrix N, $C_{noise} = G^* C_X (G^*)^T = \sigma_0^2 N$. Compared to a S-H WFS with round spots, the noise coefficients (diagonal elements of N) are somewhat larger, especially for high-order modes. As a result, the ESF grows faster and the parameter r_1 in (7) is smaller than in the case of round spots. This is only a minor factor, however, because the total variance $\sigma^2 = \sigma_0^2 \sum_j N_{j,j}$ plays the leading role in determining the corrected-mode errors, as in the case of the classical AO.

The WFS noise is filtered by the AO loop temporal controller. In the case of modal control, each mode has its own temporal response. We found that for the SAM instrument with its large LGS flux a common controller for all corrected modes works just as well. The *noise gain* factor n_g is then common to all modes, showing the attenuation (or increase) of the rms noise in closed loop compared to one loop cycle. So, $C_{noise} = n_g \sigma_0^2 N$ and the total variance σ^2 in (7) is simply proportional to $n_g \sigma_0^2$.
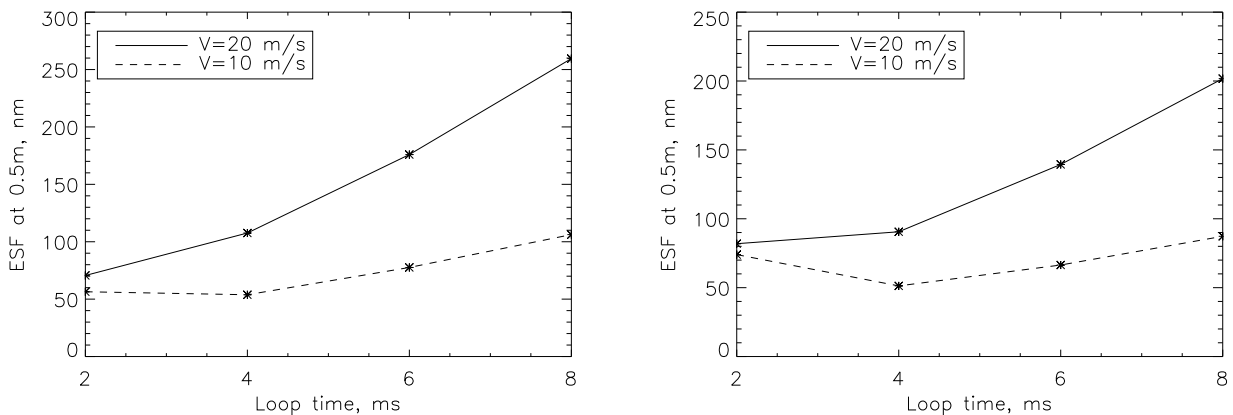
Figure 7. The ESF of corrected modes at 0.5 m baseline as a function of the loop time for spot elongation $2''$ and two controllers, integrator with gain $g = 0.6$ (left) and Smith predictor with $g = 1$, $K_s = 0.4$ (right). The solid and dotted lines correspond to the wind speed of $20\,$m/s and $10\,$m/s, respectively.

Servo lag error is determined by the loop response time and the rapidity of atmospheric turbulence. For each mode, we use a model of a single turbulent layer moving with the wind speed V, calculate the temporal spectrum, multiply it by the loop error rejection function and integrate to find the coefficients α_j that show the reduction of atmospheric variance by the AO loop. We do not calculate the temporal cross-spectrum of Zernike mode pairs, but, instead, simply assume that the cross-covariance terms of the lag error are proportional to the Noll matrix C_ϕ,

$$C_{lag} \approx (\lambda/2\pi)^2 (D/r_0)^{5/3} C_\phi \sqrt{\alpha_i} \sqrt{\alpha_j}, \tag{8}$$

The diagonal elements of the matrix C_{lag} calculated this way are correct, the off-diagonal elements are approximate.

In SAM, we can use two loop controllers: either a simple integrator or a *Smith predictor* (SP) (Ref. 1, Ch. 6). The SP controller is helpful in compensating for the delay of 2 loop cycles. We set its gain to 1 and the compensating coefficient $K_s = 0.7$. With these parameters and a 2-loop delay, $n_g = 0.87$.

Table 1. Power-law models of ESF for non-common-path aberrations

Name	j	n	m	A	α
Defocus	4	2	0	21.0	1.7
Astigmatism	5,6	2	1	14.5	1.8
Coma	7,8	3	1	21.7	1.5
Trefoil	9,10	3	3	15.6	1.6
Spherical	11	4	0	16.8	1.2
-	12,13	4	2	15.6	1.2
-	14,15	4	4	18.1	1.5

Figure 7 shows the ESF of corrected modes at $0.5\,\mathrm{m}$ baseline as a function of the AO loop time τ for the case of SAM (45 corrected Zernike modes). We take into account that the $2\,\mathrm{ms}$ loop time increases the readout noise in the WFS compared to longer exposures and that the flux is proportional to τ. The error is dominated by the servo lag, with SP controller showing better results than the integrator. A spot elongation $\Delta = 2''$ is assumed. In fact, the system performance improves at larger Δ, but the restricted WFS field does not permit us to use this advantage.

4.3 Non-common-path aberrations

Normally, non-common-path aberrations (NCPA) will be compensated by careful optical alignment and suitable offsets in the WFS. However, such compensation can be done only with finite accuracy, therefore the effect of small residual NCPA should be considered.

Each aberration affects the transfer function T_0 in Eq. 1 in a complex way. However, small aberrations cause only a slight broadening of the PSF and can be described by an additional term in the ESF. Although aberrations are deterministic rather than random, this extension of the ESF formalism helps to quantify the NCPA effect in the same way as other AO errors.

For small amplitudes of Zernike aberrations a (in microns, Noll's notation), the SF $D_{\epsilon, NCPA}(r)$ will be quadratic in a. Calculations confirm this and show that at small baselines the aberration-induced ESF averaged in azimuth is close to a power law,

$$D_{\epsilon, NCPA}(r) \approx a^2 A(r/D)^{\alpha} \tag{9}$$

This model was fitted to the radially-averaged OTFs computed for a range of aberrations and proved to be adequate, at least for the purpose of error budgeting. The powers and coefficients depend on the type of aberrations, i.e. on the radial n and azimuthal m orders (Table 1).

4.4 The effect of instrumental errors on the PSF

We give an example of the performance and error analysis for SAM in Table 2 where the PSF parameters for $0.7\,\mu\mathrm{m}$ wavelength and observations at zenith are listed for good, typical, and bad atmospheric conditions. We also calculated the uncorrected atmospheric PSFs, with and without the effect of ripple on the telescope optics. The loss of FWHM resolution caused by combined errors is 11% under typical conditions, 17% under good conditions, and 7% under bad conditions. This roughly matches the $(1 + F)$ scaling suggested above. The effect of errors is larger for the energy concentration, mostly caused by the optical ripple. Nevertheless, the errors do not "eat up" all gain provided by SAM over un-compensated PSFs, which remains very substantial.

Table 2. PSF parameters: uncorrected with ideal telescope, uncorrected with real SOAR optics, corrected by the ideal SAM instrument, and corrected with budgeted SAM errors. Observations at zenith, wavelength 0.7 μm.

Parameter	FWHM, arcsec			Energy in 0.3″ diam.		
Case	Good	Typical	Bad	Good	Typical	Bad
Atmosphere	0.449	0.554	0.684	0.203	0.143	0.099
Atm. + SOAR opt.	0.452	0.559	0.692	0.180	0.127	0.089
SAM, ideal	0.170	0.254	0.371	0.380	0.272	0.185
SAM, errors	0.200	0.282	0.396	0.301	0.218	0.150

REFERENCES

[1] F. Roddier, ed., *Astronomical Adaptive Optics,* Cambridge Univ. Press, Cambridge, 1999.

[2] A. Tokovinin, S. Thomas, B. Gregory, N. van der Bliek, P. Schurter, R. Cantarutti, E. Mondaca, "Design of ground-layer turbulence compensation with a Rayleigh beacon", *Proc. SPIE,* **5490**, pp. 870-878, 2004

[3] R.G.M. Rutten, P. Clark, R.M. Myers et al., "Facility class Rayleigh beacon AO system for the 4.2-m William Hershel Telescope", *Proc. SPIE,* **4839,** pp. 360-369, 2003

[4] J.-P. Véran, F. Rigaut, H. Maître, D. Rouan, "Estimation of the adaptive optics long-exposure point-spread-function using control loop data", *JOSA(A),* **14,** pp. 3057-3069, 1997

[5] A. Tokovinin, M. Le Louarn, E. Viard, N. Hubin, R. Conan, "Optimized modal tomography in adaptive optics", *Astron. & Astrophys.,* **378,** pp. 710-721, 2001.

[6] A. Tokovinin, "Seeing improvement with ground-layer adaptive optics", *PASP* **114,** pp. 941-951, 2004

[7] D.R. Andersen, J. Stoesz, S. Morris, M. Lloyd-Hart, D. Crampton, T. Butterly, B. Ellerbroek, L. Jolissaint L. et al., "Performance Modeling of a Wide Field Ground Layer Adaptive Optics System", *PASP,* **118,** pp. 1574-1590, 2006

[8] V. Kornilov, A. Tokovinin, N. Shatsky, O. Voziakova, S. Potatin, B. Safonov, "Combined MASS-DIMM instrument for atmospheric turbulence studies", *MNRAS,* **383,** pp. 1268-1278, 2007

[9] A. Tokovinin, T. Travouillon, "Model of turbulence profile at Cerro Pachón", *MNRAS*, **365**, pp. 1235-1242, 2006

[10] M. van Dam, A. Bouchez, D. Le Mignant et al., "The W.M.Keck Observatory Laser Guide Star Adaptive Optics System: Performance Characterization", *PASP,* **118,** pp. 310-318, 2006

[11] S. Thomas, T. Fusco, A. Tokovinin, M. Nicolle, V. Michau, G. Rousset, "Comparison of centroid computation algorithms in a Shack-Hartmann sensor", *MNRAS,* **371,** pp. 323-336, 2006